Whole system radar modelling:

Kannanthara, Jithin; Griffiths, Darren; Jahangir, Mohammed; Jones, Jonathan M.; Baker, Chris J.; Antoniou, Michail; Bell, Colin J.; Bongs, Kai; Singh, Yeshpal; White, Henry J

DOI:
10.1049/rsn2.12399

Received: 31 October 2022 | Revised: 10 March 2023 | Accepted: 15 March 2023

DOI: 10.1049/rsn2.12399

IET Radar, Sonar & Navigation

The Institution of Engineering and Technology WILEY

ORIGINAL RESEARCH

Whole system radar modelling: Simulation and validation

Jithin Kannanthara[1] | Darren Griffiths[1] | Mohammed Jahangir[2] | Jonathan M. Jones[1] | Chris J. Baker[2] | Michail Antoniou[2] | Colin J. Bell[3] | Henry White[3] | Kai Bongs[1] | Yeshpal Singh[1]

[1]School of Physics and Astronomy, University of Birmingham, Birmingham, UK

[2]School of Electronic, Electrical and Systems Engineering, University of Birmingham, Birmingham, UK

[3]BAE Systems, Farnborough, UK

Correspondence

Jithin Kannanthara.
Email: jxk902@student.bham.ac.uk

Funding information

Horizon 2020 Framework Programme, Grant/Award Number: 820404; UK National Quantum Technology Hub in Sensing and Timing, Grant/Award Number: EP/T001046/1; BAE systems

Abstract

The ever-expanding horizon of radar applications demands solutions with high-end radar functionalities and technologies and is often limited by the available radar equipment, cost and time. A practical method to tackle the situation is to rely on the modelling and simulation of radar systems based on the user requirements. The comprehensive system-level modelling of a pulsed Doppler radar in MATLAB/Simulink consisting of all the fundamental blocks in the transmit chain, the environment, the receive chain, and the data processing chain is presented in this article. The first half of the article discusses the high-fidelity simulation of each building block in the radar model. In the second half of the article, the range-Doppler plot generated from the high-fidelity radar model is compared and validated using the range-Doppler plot from a real radar trial. The radar phase noise plays a crucial role in the detection of slowly moving, low radar cross-section targets in the presence of strong clutter. The article also briefly discusses the effects of radar oscillator phase noise in the range-Doppler plot. The validated, fully flexible radar model has the advantage of supporting the addition of further building blocks and optimising the parameters based on user requirements.

KEYWORDS

Doppler radar, modelling, oscillators, phase noise, radar receivers, radar signal processing, radar transmitters, thermal noise

1 | INTRODUCTION

Radars are used for a wide variety of applications in the fields of meteorology [1, 2], healthcare [3–5], mapping and astronomy [6, 7], law enforcement [8], and defence [9–13]. It is impossible to fully test a complex radar system across all hardware and environmental combinations in the real world. One possible solution to test the radars would be to model the radar hardware and environment based on the user requirements and radar applications. At best, a subset of the conditions can be tested, and the results can be used to validate more extensive radar modelling.

Over the years, there have been attempts to model the different aspects of the radar. The development of phase noise theory and a new design equation for the phase noise level in frequency-modulated continuous wave radar and its validation with real data was discussed in refs. [14, 15]. A relatively simple method for precise simulation of the geometry of objects in the environment in synthetic aperture radar was proposed in ref. [16]. The environment modelling in radar literature was mainly focussed on the radar performance in the coherent and non-coherent radar sea clutter [17–20]. A hardware-in-the-loop simulator for radar targets based on scattering model theory was discussed in ref. [21].

Even though there are different cases of radar modelling in the literature, each radar model focuses on a specific aspect of radar. The specific aspect could be modelling the radar environment or modelling a limited number of building blocks in a radar. In recent years, there has been very little literature on radar hardware and radar system modelling. An incoherent scatter radar simulation system using a modular design concept was discussed in ref. [22], and an introductory simulation of a

pulsed Doppler radar system using MATLAB and Simulink was discussed in ref. [23]. A signal level simulator consisting of algorithms for the simulation of raw radar return signals was discussed in ref. [24]. The literature lacks a high-fidelity radar model with all the building blocks that could be used to examine and predict each radar building block's performance and fundamental limitations.

The phase noise in radars is due to the random fluctuation of the phase of the radar oscillator [25]. In range-Doppler plots, the phase noise floor emerges out of the thermal noise floor for range bins with strong clutter power. The increase in the noise floor due to the phase noise degrades the available signal-to-noise ratio (SNR) for target detection. Target detection becomes more difficult for slowly moving low radar cross-section (RCS) targets like drones.

The novel radar model developed and discussed in this paper is a comprehensive model that consists of all the fundamental building blocks in the transmit chain, the receive chain, the data processing chain and the environment of a pulsed Doppler radar. The radar model focuses on the fidelity of every radar hardware block in the simulation. The high-fidelity radar model is also validated by comparing the range-Doppler plot generated from the model with the range-Doppler plot from an actual radar trial. The effect of oscillator phase noise in the range-Doppler plot and in target detection is also briefly explored. The radar model discussed in this paper can integrate further building blocks and optimise every parameter in each building block to potentially replicate any radar design.

This paper is organised as follows. In the theory and simulation section, we discuss the theory behind each radar building block and the realisation of each building block in the simulation. We have also provided the mathematical model of the signal and the SNR at the output of each building block. In the results and validation section, we describe the generation of range-Doppler data from the simulated radar model. We then validate the simulated model and the range-Doppler plot with the range-Doppler data processed from real radar trials. Finally, in conclusion, we summarise the research presented in the paper.

2 | THEORY AND SIMULATION

Any generic radar design consists of a transmit chain to generate and transmit the signal, a receive chain to receive the reflected signal from the environment and a data processing chain to process the received signal. The frequency of operation of the radar, the constituent blocks within the radar and the parameters and power budgets depend on the radar application. The radar model discussed in the paper is based on Gamekeeper 16 U [26] staring radar with further simplifications. The model built in the MATLAB/Simulink framework can modify and optimise all the parameters at the component level and include further building blocks. The schematic of the front end of the monostatic radar model is given in Figure 1.

The radar model can be subdivided into four major sections: transmit chain, receive chain, the data processing chain, and the environment. The building blocks within the transmit chain, environment, and receive chain were represented as separate system-level blocks in Simulink, with each Simulink block containing further sub-blocks. All the building blocks were modelled in such a way that the output of one block was connected to the input of another block with test probes placed in between. The test probes were used to analyse the input and output of each building block in the model. The data

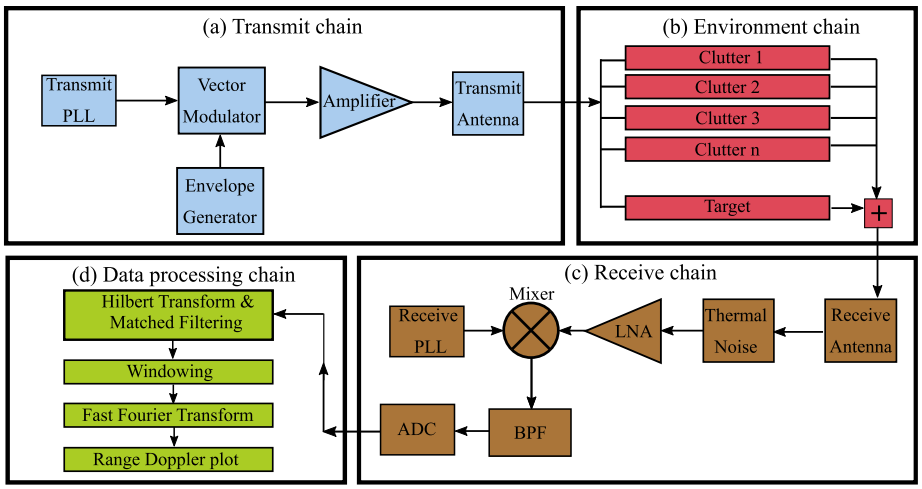

FIGURE 1 Schematic of the front end model of the monostatic radar in simulation. The front end consists of four main sections. The transmit chain transmits the pulsed sinusoidal signal to the environment through the transmit antenna. The clutter and targets in the environment reflect the signal to the radar receive antenna. In the receive chain, the received signal undergoes stages of amplification and down-conversion to generate an intermediate frequency signal. The intermediate frequency signal gets converted to a baseband signal in the data processing chain. The baseband signal undergoes further data processing stages to enhance the target's signal-to-noise ratio. The building blocks in the transmit chain, the environment chain, and the receive chain are modelled as separate blocks in Simulink. The building blocks in the data processing chain were generated using a separate code written in MATLAB.

at the output of the last block of the receive chain was taken to the MATLAB workspace. A separate code was written in MATLAB for the data processing chain and the generation of the range-Doppler plot.

2.1 | Transmit chain

The first block in the transmit chain of the model is the transmitter phase lock loop (transmit PLL) and is one of the most crucial blocks in the radar simulation. Generally in radar hardware, the radar oscillator signal at the reference frequency is up-converted to a radio frequency signal at the required transmit frequency using a frequency up-converter. The frequency up-converter could be a PLL or a frequency mixer. In the model, the transmit PLL was used to directly generate a continuous sinusoidal wave at a specific L band transmit frequency. The transmit PLL in the model acts as a direct digital synthesiser to generate the required transmit frequency. The model currently has a simplified version of the signal generator, and further blocks can be integrated to represent a separate radar oscillator and PLL up-converter. The transmit PLL has the further potential to integrate blocks to model square pulses or frequency-modulated waveforms at any transmit frequency and amplitude, depending on the requirements of the radar model.

The phase noise is inherent to any radar oscillator. In the model, the equivalent phase noise at the transmit signal can be included. The phase noise of any oscillator at any frequency can also be simulated in the transmit PLL block by providing the respective oscillator's frequency offset and the phase noise level. In the phase noise modelling discussed later in the paper in Section 3.3, the equivalent oscillator phase noise at the transmit frequency is added to the simulation.

The mathematical model of the sinusoidal signal at the output of the transmit PLL is given by,

$$S_{PLL}(t) = A_{PLL}\cos[2\pi f_T t + \theta], \tag{1}$$

where $S_{PLL}(t)$ represents the sinusoidal signal at the output of the transmit PLL, A_{PLL} represents the amplitude of the signal at the output of the PLL, θ represent the phase of the signal, and f_T represents the transmit frequency.

The model's continuous sinusoidal wave generated at the transmit PLL was converted to a pulsed signal using a vector modulator. The vector modulator was a mixer that added the amplitude envelope to the output of the transmit PLL. The envelope generator provided the specific amplitude envelope to the vector modulator. The envelope generator can generate a rectangular envelope or any shaped amplitude envelope depending on the requirements of the radar model. In the model, the generated envelope was a shaped pulse with a pulse width of about 1 μs and a pulse repetition interval (PRI) of about 136 μs. The mathematical model of the signal at the output of the vector modulator is given by,

$$S_V(t) = A_V \cos[2\pi f_T t + \theta], \tag{2}$$

where $S_V(t)$ represents the pulsed signal at the output of the vector modulator and A_V represents the amplitude of the signal at the output of the vector modulator.

The amplifier was used to amplify the vector modulator output signal. The amplifier block has the potential to amplify the signal to any value of transmitted power, the power at the output of the transmit amplifier. The mathematical model of the signal at the output of the amplifier is given by,

$$S_A(t) = A_A \cos[2\pi f_T t + \theta], \tag{3}$$

where $S_A(t)$ represents the signal at the output of the amplifier and A_A represents the amplitude of the signal at the output of the amplifier.

In real radar, the transmit antenna is used to transmit the real electromagnetic signal at the output of the amplifier to the environment. There are different transmit antenna architectures, and the transmit antenna generated in the model was a simplified antenna with a single transmitter and a constant antenna gain. In the model, the transmit antenna output was connected to the input of the environment model. The mathematical model of the transmitted signal is given by [27, 28],

$$S_T(t) = A_T \cos[2\pi f_T t + \theta], \tag{4}$$

where $S_T(t)$ represents the transmitted signal, A_T, f_T, and θ represents the amplitude, frequency, and phase of the transmitted signal respectively. Even though the transmit signal is a pulsed signal, for simplicity, the time dependency of the pulse is not explicitly mentioned in Equation (4). Hence Equation (4) is a simplified model of the real-valued transmitted signal. The Equations (1)–(4) are also connected to one another as $S_V(t)$ is a function of $S_{PLL}(t)$, $S_A(t)$ is a function of $S_V(t)$, and $S_T(t)$ is a function of $S_A(t)$.

2.2 | Environment

For a real radar, the environment consists of clutter that are stationary objects, including buildings, trees, and other geographical features in the field of view. The environment also consists of moving targets, including drones, aircraft, ships, and birds. The transmitted signal gets reflected by the objects in the environment and reaches the receive antenna of the radar. In radar theory, the radar range equation is used to determine the power of the received signal and is given by,

$$P_R = \frac{P_T G_T G_R \lambda^2 \sigma}{4\pi^3 R^4}, \tag{5}$$

where P_R is the received signal power, P_T is the transmitted signal power, G_T and G_R are the transmit antenna gain and the receive antenna gain respectively, λ is the wavelength of the transmitted signal, σ and R are the RCS and the target range respectively. The received signal power is the power of the received signal at the output of the receive antenna.

In the model, a simple representation of the magnitude response of both the target and the clutter was realised. The signal from the transmit chain was directed to object blocks representing clutter and targets. Algorithms following the radar range equation were performed to specify each object's range, the RCS, and the Doppler velocity. The objects were placed at the radar bore-sight and can potentially include additional algorithms to place objects at a specific angle in the azimuth and elevation. The reflected signal from the object blocks was directed to the receive chain.

2.3 | Receive chain

In a real radar, the reflected signal from the objects in the environment is detected at the receive antenna. The receive antenna can be of different configurations, either a single antenna or a combination of many phased array antenna elements. In the model, the receive antenna was a single antenna with a constant antenna gain which is used as a simplified representation even in the case where the model is compared with a multiple receive array system.

Consider a radar that transmits a series of M pulses with $0 \le m \le M-1$, separated by a PRI of T. For a target with an initial range of R_o and a velocity of ν, the range of the target for the mth transmitted pulse is $R_o - \nu mT$. For the mth transmitted pulse, the signal that reaches the receiver antenna will have a time delay equivalent to $\frac{2}{c}(R_o - \nu mT)$. The mathematical model for the delayed received signal is given by,

$$\begin{aligned} S_R(t) &= S_T\left(t - \frac{2}{c}(R_o - \nu mT)\right), \\ &= A_R \cos\left[2\pi f_T t + 2\pi\left(\frac{2\nu}{\lambda}\right)mT + \left(\theta - \frac{4\pi R_o}{\lambda}\right)\right], \end{aligned} \tag{6}$$

where $\frac{2\nu}{\lambda} = f_d$ is the Doppler frequency of the target moving towards the radar and $\theta - \frac{4\pi R_o}{\lambda} = \theta'$ is the phase of the received signal. A_R represents the amplitude of the received signal and follows the radar range equation.

Since the received signal power of the radar target is weak compared to both clutter and noise, the challenge is to bring the signal power considerably above the noise floor. The SNR describes the signal power over the noise floor. The SNR is generally represented in dB. The noise provides the statistical basis for the target detection; hence, controlling noise within the radar receive chain is critical. The sources of noise in radars are both internal and external. One of the internal noise sources in radars is thermal noise. Phase noise can also be a significant source of noise in some radar systems.

In the simulated radar model, the phase noise was integrated into the transmit PLL block of the transmit chain. The thermal noise is due to the thermal agitation of the electrons in the receive chain elements. The thermal noise is random, and the power spectrum of the thermal noise is uniform and flat across all frequencies [29]. The model used the thermal noise block to generate and add complex thermal noise to the real valued received signal. The thermal noise consisted of both positive and negative frequencies. The mathematical equation for the thermal noise is given by,

$$N = k_B T B, \tag{7}$$

where N, k_B, T, and B represent the noise power, Boltzmann's constant, noise temperature, and noise bandwidth respectively.

The thermal noise block can model any value of temperature. In the model, the temperature was kept at room temperature of 290 K. The noise bandwidth in the thermal noise block was equivalent to the sampling frequency used in the radar simulation. The sampling frequency was kept at 5 GHz and was at least two times higher than any of the frequencies generated in the radar model.

The SNR of the received signal (SNR_R) for a received signal power of P_R from Equation (5) and a noise power of N from Equation (7) is,

$$SNR_R = \frac{P_T G_T G_R \lambda^2 \sigma}{4\pi^3 R^4 k T B}. \tag{8}$$

The low noise amplifier (LNA) is a special kind of amplifier that amplifies the weak received signal without drastically degrading the SNR. The LNA noise figure (NF) is the parameter that quantifies the degradation of SNR by the LNA. The LNA was modelled as an amplifier with a specific NF. The LNA amplifies both the signal and the noise. The noise power gets further amplified by the NF of the LNA. The LNA model can specify any user-required value for the amplification and the NF. The SNR at the output of the LNA (SNR_{LNA}) is given by,

$$SNR_{LNA} = SNR_R - NF. \tag{9}$$

The mathematical model for the received signal at the output of LNA (S_{LNA}) is given by,

$$S_{LNA}(t) = A_{LNA} \cos[2\pi f_T t + 2\pi f_d m T + \theta'] \tag{10}$$

where A_{LNA} represents the amplitude of the received signal after the LNA.

In a real radar, the output of the LNA is mixed down to a convenient intermediate frequency (f_{IF}) using a mixer. The mixer has two inputs, an RF and a local oscillator (LO) input. The RF input of the mixer takes the output of the LNA as shown in Equation (10). The LO input of the mixer is generally a local oscillator output at a frequency equivalent to $f_T + f_{IF}$. The mathematical model for the sinusoidal signal at the output of local oscillator is given by,

$$S_{LO}(t) = \cos[2\pi(f_T + f_{IF})t]. \tag{11}$$

The output of the mixer consists of two frequencies, the first corresponding to the sum of the two input frequencies and the

second corresponding to the difference between the two input frequencies. The difference between the two frequencies is equivalent to the f_{IF}. The ratio between the input RF power and the output IF power is known as the mixer conversion loss. For an ideal mixer with a LO input amplitude of unity and the RF input amplitude of A, the conversion loss is 6 dB [30, 31]. The conversion loss affects both the signal and the noise. The effective SNR gain due to the conversion loss in a mixer is zero.

The NF of the mixer (NF_{MXR}) is another parameter that affects the SNR. There is also an undesired frequency band known as the image frequency for a mixer that down-converts the RF to IF using the LO, along with the desired frequency band. The noise will be present in both the desired and the undesired band for a real-valued signal accompanied by a complex-valued thermal noise. The down-conversion folds back the noise in the image band on top of the noise in the desirable band. The SNR at the output of the mixer SNR_{MXR} is given by,

$$SNR_{MXR} = SNR_{LNA} - NF_{MXR}. \tag{12}$$

A narrow bandwidth band-pass filter (BPF) is placed after the mixer to transmit the difference frequency centred at f_{IF}. The signal power at the output of the BPF is equivalent to the signal power at the input of the BPF. The noise power at the output of the BPF is reduced by a factor of B/B_{BPF}, where B is the noise bandwidth before the BPF and B_{BPF} is the bandwidth of the BPF. The SNR at the output of the BPF (SNR_{BPF}) is given by,

$$SNR_{BPF} = SNR_{MXR} + 10log_{10}\left(\frac{B}{B_{BPF}}\right). \tag{13}$$

The mathematical model for the signal at the output of the band-pass filter (S_{BPF}) is given by,

$$S_{BPF}(t) = \frac{A_{LNA}}{2}\cos[2\pi f_{IF}t + 2\pi f_d mT + \theta'], \tag{14}$$

where $\frac{A_{LNA}}{2} = A_{BPF}$ is the amplitude of the signal after the BPF.

In the simulation, the mixer block performs the mixing operation between the noisy received signal at the output of LNA and the receive PLL output signal. The receive PLL generated a continuous sinusoidal wave at a specific L band frequency. The receive PLL can be modified to generate signals at any required frequency. The output of the mixer consisted of both the sum and the difference frequency. The BPF was placed after the mixer to transmit the difference frequency centred at the f_{IF}.

An analogue-to-digital converter (ADC) is generally used to convert the analogue signal to a digital signal. The ADC can also perform signal down-conversion through frequency aliasing. Since the model was already in the digital domain, the ADC block in the model was used to generate a down-converted frequency signal.

In the simulation, the f_{IF} was sampled at a specific ADC clock frequency (lower than the f_{IF}) to generate aliased signals at second intermediate frequency (f_{IF2}). The ADC for aliasing was realised using a signal-to-workspace block sampled at the clock frequency. The output of the ADC was a sinusoidal signal at f_{IF2}. The ADC has the potential to add further blocks to generate quantisation noise. The ADC in the simulation does not alter the SNR, and hence the SNR at the output of the ADC becomes:

$$SNR_{ADC} = SNR_{BPF}. \tag{15}$$

The mathematical model of the signal at the output of the ADC is given by,

$$S_{ADC}[t] = A_{ADC}\cos[2\pi f_{IF2}t + 2\pi f_d mT + \theta'], \tag{16}$$

where A_{ADC} is the amplitude of the signal after the ADC and is equivalent to the signal amplitude before ADC. The signal-to-workspace block carried the Simulink data to the MATLAB workspace. The further processing of the data was performed in MATLAB.

2.4 | Data processing chain

The first and foremost step in data processing was the down-conversion to baseband and matched filtering. There are several methods for down-conversion. In the model, we use the Hilbert transform. Theoretically, the Hilbert transform generates the complex baseband signal containing the in-phase and the quadrature components. The simplified mathematical model of the baseband complex signal at the output of the Hilbert transform is given by,

$$S_{HT}[t] = A_{HT}\exp[2\pi f_d mT + \theta'], \tag{17}$$

where A_{HT} is the signal's amplitude after the Hilbert transform. The complex baseband radar signal is used to measure the phase and amplitude independently [28].

The matched filter is a linear filter based on the principle of correlation in the time domain between the noisy received signal and the reference signal to improve the SNR. For an ideal matched filter, maximum SNR is obtained when the reference signal is a time-delayed mirror image of the received signal [32]. For a matched filter that provides an SNR gain of G_{MF}, the SNR at the output of the matched filter (SNR_{MF}) is given by,

$$SNR_{MF} = SNR_{ADC} + G_{MF}. \tag{18}$$

The mathematical model of the signal at the output of the matched filter is given by,

$$S_{MF}[t] = A_{MF}\exp[2\pi f_d mT + \theta'], \tag{19}$$

where A_{MF} is the amplitude of the signal at the output of the matched filter.

In the simulation, the real-valued signal at f_{IF2} was converted to a complex signal at the baseband. The matched filtering was performed to improve the SNR. The matched filter coefficient was derived from the simulated transmit signal.

The Fast Fourier transform (FFT) is used to convert the signal in the time domain to the frequency domain, thereby providing the signal's frequency information. For a measured signal, the discontinuities due to the non-integer number of periods result in frequency components leaking into adjacent frequency bins. The leakage causes the fine spectral lines in FFT to spread and is known as spectral leakage [33]. The spectral leakage is minimised by a technique known as windowing. The windowing multiplies the measured time domain discontinuous signal with an amplitude envelope that approaches zeros at both ends [34]. The SNR at the output of the windowing is degraded by a factor known as the loss factor (LF). The loss factor is defined as the ratio of the maximum achievable SNR (SNR without windowing) to the actual SNR (SNR with windowing) [35]. The SNR at the output of windowing (SNR_W) is given by,

$$SNR_W = SNR_{MF} - LF. \tag{20}$$

In real radar, the FFT extracts the Doppler frequency/Doppler velocity information of both the targets and clutter. The data at the input of the FFT also undergo coherent pulse integration. For a coherent integration of N pulses, the power in the integrated signal component is increased by N^2 and the integrated noise power is increased by N. Hence, the effective increase in the SNR is N in dB. The SNR at the output of the FFT is given by,

$$SNR_{FFT} = SNR_W + N. \tag{21}$$

Blackman-Harris windowing and a 2048-point FFT were applied to the matched filter output in the simulation. The processed signal in the frequency space is generally represented as range-Doppler plots, with the vertical axis representing the range of the radar and the horizontal axis representing the target's frequency (radial velocity). The data after the FFT was represented in the simulation as a range-Doppler plot.

3 | VALIDATION OF RADAR MODEL

Validating the radar model is as crucial as developing the comprehensive radar model. The best method to compare and validate a simulated radar model with a real radar is by comparing the range-Doppler plots emphasising the crucial figures of merit. For a range-Doppler plot, either real or simulation, the significant figures of merit are the SNR and the clutter to noise ratio (CNR).

The comprehensive radar model presented in the paper has the advantage of simulating clutter and targets at user-specified ranges and RCS. The targets and clutter are modelled as point scatters in the simulation. A range-Doppler plot for a full coherent processing interval (CPI) was simulated to validate the model. The CPI consisted of 2048 pulses, each with a PRI of about 136 μs. The range-Doppler plot was generated by performing FFT along the slow time axis. The slow time axis consists of all the PRIs within a CPI. The simulated range-Doppler plot was compared with a real range-Doppler plot from a radar trial. The real range-Doppler plot consists of a number of range bins and 2048 Doppler bins.

A three-level validation was performed. In the first level of validation, the system-level signal powers and the SNR values at the output of the different blocks of the simulation were compared with the expected values. In the second level of validation, the basic parameters from the simulated range-Doppler plot were compared with the real radar values. In the third level of validation, the CNR, the SNR, the thermal noise floor, and the phase noise floor from the range-Doppler plot for both the simulation and real data were compared.

3.1 | Comparison of system level signal power and SNR

In the first level of validation, the signal power and the SNR at different stages within the transmit chain, the receive chain, and the data processing chain were considered. In the first level of validation, a single stationary clutter was kept at a range of 600 m and an arbitrary value of RCS. The simulation for a full CPI was performed. The test probes at the output of each building block of the radar model were used to evaluate the signal power, the noise power, and the SNR values. The first stage of validation is conveniently divided into two parts. The first part compares the signal powers, and the second part compares the SNR values.

In the first part, the simulated signal power at the output of the transmit amplifier, the transmit antenna, and the receive antenna is compared with the expected values. The expected value of the signal power at the output of the transmit amplifier and the transmit antenna was taken from the Gamekeeper 16 U power budget. The expected value of the signal power at the output of the receive antenna was calculated from the radar range equation (Equation 5). Table 1 compares the simulated and the expected value of signal powers. We can clearly see that the simulated and the expected signal power are in very close agreement. The thermal noise was added to the received signal at the output of the receive antenna. The thermal noise power

TABLE 1 Simulated and expected values of signal powers at the output of different radar building blocks.

Radar block	Simulated (dB)	Expected (dB)	Difference (dB)
Transmit amplifier	33.0	33.0	0.0
Transmit antenna	45.4	45.5	0.1
Receive antenna	−74.5	−74.4	0.1

generated by the thermal noise block was expected and obtained at −107 dB.

In the second part, the simulated SNR at the output of each building block in the receive chain and the data processing chain was compared with the expected values. The signal power and the thermal noise power at the output of each building block were used to calculate the simulated SNR values. The expected SNR values were calculated using a combination of radar theory and power budget reference values. The SNR values at the outputs of different blocks are summarised and compared in the Table 2. Table 2 clearly shows a good parity between the simulated and the expected SNR values at the output of every building block. The Tables 1 and 2 show the fidelity of every building block in the simulated whole system radar model.

3.2 | Comparison of range and Doppler basic parameters

In the second level of validation, the basic parameters from the simulated range-Doppler plots were compared with the parameters from the real radar. At first, a range-Doppler plot with thermal noise was simulated with a single stationary clutter and a single moving target, placed at a distance of 600 and 1500 m respectively. The range and RCS values were arbitrary and did not follow a specific reference. The target's velocity was kept at 251 Hz, equivalent to 30 m/s for the specific L band transmit frequency.

The simulated range-Doppler plot consisted of a number of range bins. The PRF of the simulated range-Doppler plot was equivalent to the real radar range-Doppler plot. Figure 2 shows the simulated range-Doppler plot with the range bin on the vertical axis and the Doppler frequency on the horizontal axis. Figure 2 clearly shows a stationary clutter (highlighted in green) with a zero Doppler and a target (highlighted in red) with a Doppler frequency of around 251 Hz.

The range bin and the Doppler bin for both the target and the clutter were measured from the simulated range-Doppler plot in Figure 2. The radar range and Doppler resolution were also measured from the simulated plot. The second level of validation was performed by comparing the basic parameters, including the range bin, Doppler bin, range resolution, and Doppler resolution for both the simulated radar and the real radar. The range resolution for the simulated and real radar was in very good agreement. The comparison of the remaining parameters is summarised in the Table 3.

The expected range resolution and Doppler resolution were taken from a prototype staring radar. The expected range bin and Doppler frequency bin for both the clutter and the target were calculated from the range and Doppler velocity provided in the simulation, using the range resolution and Doppler resolution reference values. The simulated values were the values measured from the simulated range-Doppler plot. Table 3 clearly shows that the basic parameters from the simulation are very close to the expected parameters from the real radar. The radar model discussed in the paper can be tuned to simulate all the basic parameters, including the range resolution, Doppler resolution, CPI, and PRF, to any required configuration.

(a) Simulated range-Doppler plot without the oscillator phase noise. The plot consists of the stationary clutter and a single simulated target in the uniform thermal noise floor.
(b) Simulated range-Doppler plot with the oscillator phase noise. The plot consists of the stationary clutter and a single simulated target in the overall noise floor. The overall noise floor consists of phase noise and thermal

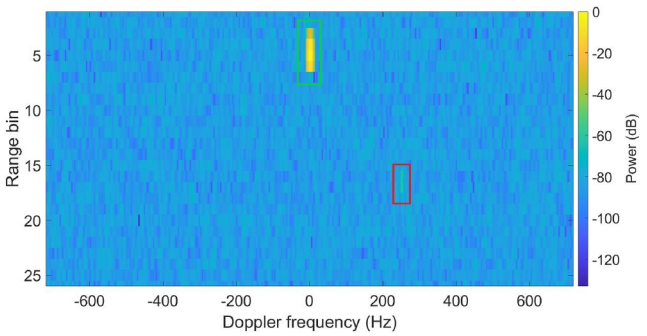

FIGURE 2 Simulated range-Doppler plot with range bin in the vertical axis and Doppler frequency in the horizontal axis. The spectrum is shown for −700 to +700 Hz. The single stationary clutter and the single Doppler target are highlighted within a green and red box respectively. The range-Doppler plot is normalised to the clutter.

TABLE 2 Simulated and expected values of SNR at different stages in receive chain and data processing chain building blocks.

Radar block	Simulated (dB)	Expected (dB)	Difference (dB)
Before LNA	32.5	32.6	0.1
After LNA	28.0	28.1	0.1
After mixer	25.0	25.1	0.1
After BPF	45.0	45.1	0.1
After ADC	45.0	44.8	−0.2
After matched filter	59	57.8	−1.2
After windowing	55.5	54.7	−0.8
After FFT	88.6	87.8	−0.8

TABLE 3 Simulated and expected values of range and Doppler basic parameters.

Parameter	Simulated	Expected
Clutter range bin	5	5
Target range bin	17	17
Clutter Doppler bin	0	0
Target Doppler bin	70	70
Doppler resolution (Hz)	3.58	3.59

noise. The phase noise floor emerging out of the thermal noise floor for range bins with higher clutter is clearly visible.

(c) Real range-Doppler plot from the radar trial at an airfield. The phase noise floor can be seen emerging out of the thermal noise floor for range bins with higher clutter. The plot also consists of other unwanted targets as seen by the radar.

3.3 | Comparison of range-Doppler plots

In the third level of validation, the CNR, the SNR, the thermal noise floor, and the phase noise floor from the simulated range-Doppler plot are compared and validated with a real range-Doppler plot. For the third level of validation, the range-Doppler plot of a real radar trial was taken as a reference. The real radar trial was performed using the Gamekeeper 16 U in an airfield with a controlled drone (target of interest) flying on a predefined path. The range-Doppler plot consisted of a single frame equivalent to a full CPI from the radar trial with the drone. For the selected frame, the drone flew at a specific distance and at a radial velocity of 8.3 m/s towards the radar. Even though the radar trial was performed in a rural environment, the range-Doppler plot consists of other unwanted targets in the radar's field of view.

The third level of validation was performed by replicating the real range-Doppler plot in the simulation. As a first step, a range-Doppler plot was simulated with the CNR of the simulation in parity with the CNR from the real range-Doppler plot. The clutter power from an individual range bin leaks to the adjacent range bins making it impossible to generate a replica of the real CNR for every range bin in the simulation. In the first step, the thermal noise was considered to calculate the CNR for both the real and simulated range-Doppler plots.

Table 4 compares the CNR from the simulated range-Doppler plot with the CNR from the real range-Doppler plot for different range bins. Table 4 shows a good agreement between the simulated and real CNR. Since the exact replica of the real CNR cannot be generated in the simulation, a difference of a few dB between the simulated and real CNR is expected.

TABLE 4 Clutter to Noise Ratios from simulated and real range-Doppler plots for different range bins.

Range bin	Simulated CNR (dB)	Expected CNR (dB)	Difference (dB)
A	103.43	105.72	2.29
B	94.96	90.13	−4.33
C	93.89	91.92	−1.97
D	96.85	96.78	−0.07
E	65.24	64.79	−0.45
F	73.19	72.79	−0.4

The second step added the target information to the simulated range-Doppler plot. In the simulation, the target drone was realised as an object at a distance equivalent to the range of the target. The Doppler frequency of the target was kept at 69.8 Hz, equivalent to the velocity of 8.3 m/s. The RCS of the drone was modelled such that the SNR of the simulation is comparable with the SNR of the real data [36].

For any real radar, phase noise plays a significant role in detecting targets. The radar system's phase noise causes the range-Doppler plot's phase noise floor to emerge out of the thermal noise floor in range bins with stronger clutter power. The increase in the overall noise floor makes the detection of targets difficult. One great advantage of the sophisticated radar model discussed in the paper is the ability to add oscillator phase noise in the simulation. The simulation included a phase noise profile equivalent to the measured phase noise for the radar transmit signal.

The range-Doppler plot generated in the simulation is compared with the real range-Doppler plot and is given in Figure 3. All the range-Doppler plots in Figure 3 are normalised to the strongest clutter, the clutter present in the second range bin. The first two figures, Figure 3a,b, shows the simulated range-Doppler plots. Figure 3a is the simulated plot without the oscillator phase noise, and Figure 3b is the simulated plot with the oscillator phase noise. The real range-Doppler plot is given in Figure 3c.

Comparing Figure 3a,b, the increase in the overall noise floor and the emergence of the phase noise floor over the thermal noise floor is clearly visible at ranges with extremely high clutter. The clutter-induced phase noise due to large clutter backscatter is common to any radar system. The increased overall noise floor makes detecting slowing moving and low RCS targets difficult.

Figure 3b shows the simulated replica of the range-Doppler plot in Figure 3c. Qualitatively, the simulated plot looks very similar to the real range-Doppler plot. Since the CNR for every range bin cannot be exactly replicated in the simulation, the overall noise floor for every range bin separately does not match.

The target of interest is highlighted inside a red box for all the range-Doppler plots in Figure 3. In all three cases, the target appears at the 19th range bin and 19th Doppler bin. The SNR of the target was calculated from simulated and real range-Doppler plots and is given in the Table 5. Table 5 shows an excellent agreement between the simulated and the real SNR.

The peak clutter power, average thermal noise power and average overall noise power for each range bin were taken from the Figure 3b,c to generate a range-Doppler statistics graph. The range-Doppler statistics graph in Figure 4 compares the simulated and the real range-Doppler plot from the Figure 3b,c respectively.

Figure 4 clearly shows the overlapping thermal noise floor for both the real and simulated range-Doppler plots. The statistics graph shows a good agreement between the simulated and real clutter power. The clutter power for the range bin 21 from the real range-Doppler plot was an exception which

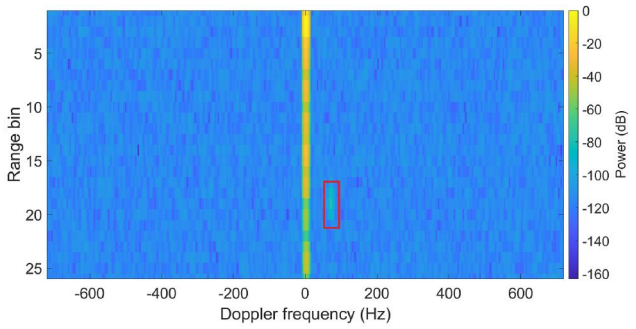

(a) Simulated range-Doppler plot without the oscillator phase noise. The plot consists of the stationary clutter and a single simulated target in the uniform thermal noise floor.

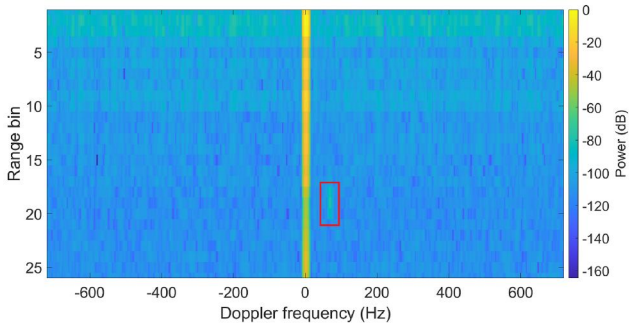

(b) Simulated range-Doppler plot with the oscillator phase noise. The plot consists of the stationary clutter and a single simulated target in the overall noise floor. The overall noise floor consists of phase noise and thermal noise. The phase noise floor emerging out of the thermal noise floor for range bins with higher clutter is clearly visible.

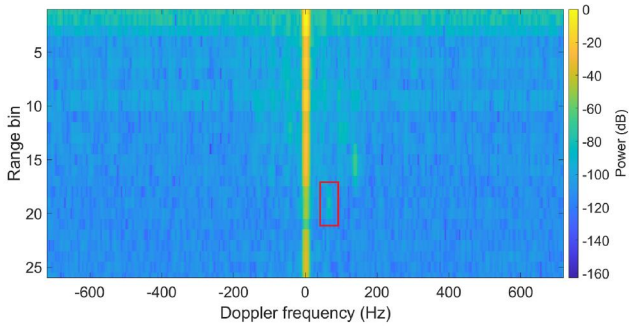

(c) Real range-Doppler plot from the radar trial at an airfield. The phase noise floor can be seen emerging out of the thermal noise floor for range bins with higher clutter. The plot also consists of other unwanted targets as seen by the radar.

FIGURE 3 Comparison of the simulated range-Doppler plots with the real range-Doppler plot. All the range-Doppler plots are normalised to the strongest clutter. The target is highlighted in the red box. The target is present across all three plots in the same range and Doppler bin. The effect of radar phase noise can be seen in the range-Doppler plots with the phase noise. The simulated range-Doppler plot with phase noise and the real range-Doppler plot show a good level of similarity.

could not be replicated in the simulation. The statistics graph also shows a close correspondence between the phase noise power for the real and simulated data within an offset of a few

TABLE 5 The calculated SNR from the simulated and the real range-Doppler plots.

Parameter	Simulated	Real
Signal to noise ratio (dB)	33.17	32.34

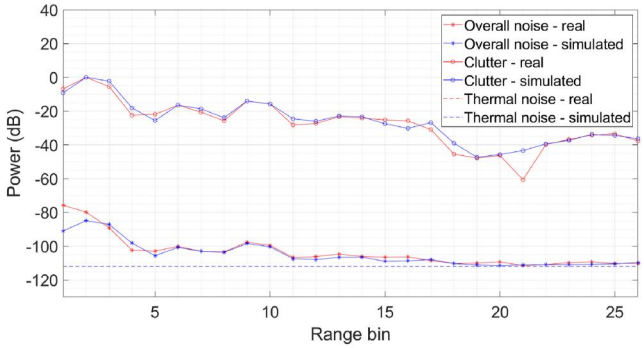

FIGURE 4 The range-Doppler statistics graph shows the clutter power, average thermal noise power, and average overall noise power for every range bin. The statistics graph consists of data from the real and simulated range-Doppler plots with phase noise. The clutter power and overall noise power for both the simulation and real data overlap to a good extent. The thermal noise floor in the simulation fully overlaps with the real data and hence is not differentiable. At the range bin with the highest clutter power, the phase noise floor is raised at least 25 dB above the thermal noise floor. The clutter-induced phase noise due to large clutter backscatter is a generic radar issue.

dB. The statistics graph shows a considerable increase in the overall noise power due to the radar oscillator phase noise. For the second range bin with the highest clutter power, the noise power is increased by at least 25 dB. Figures 3b,c, and 4 show the confidence and the fidelity of the comprehensive radar model discussed in the paper and validate the preliminary results.

4 | CONCLUSION

We have presented the modelling and simulation of a whole system radar model. The high-fidelity radar model consisted of all the fundamental building blocks within the transmit chain, the environment, the receive chain and the data processing chain of a pulsed Doppler radar. A simplified mathematical signal model and a very detailed system-level SNR model were also presented. The radar model was validated at three levels. In the first level, the signal power and SNR values at the output of each radar building block in the simulator were compared with the expected values. In the second level, the range bin, Doppler bin, range resolution, and the Doppler resolution obtained from the simulated range-Doppler plot were compared with the real radar data. In the third level, the thermal noise floor, the overall noise power consisting of both the thermal noise and the phase noise, the clutter power, the CNR and the SNR from the simulated range-Doppler plot was compared with the range-Doppler plot from a real radar trial.

In all three levels of validation, the simulated values were in good parity with the expected values.

Comparing the simulated range-Doppler plot with only the thermal noise and with both the thermal noise and the phase noise, we can clearly see that the phase noise causes the overall noise floor to rise above the thermal noise floor. The clutter-induced phase noise is common to all radar systems. For the range bins close to the radar, the overall noise floor sits at least 25 dB above the thermal noise floor. We lose a dB of margin for efficient target detection for every dB increase in the phase noise floor above the thermal noise floor. Improving the phase noise characteristic of the radar oscillator could ideally reduce the range-Doppler plot phase noise floor and thus improve the SNR available for target detection. An oscillator with lower phase noise could be really helpful in detecting slow-moving targets with very low RCS.

The radar model discussed in the paper has the advantage of accommodating further building blocks and optimising every parameter within each building block to represent any radar in great detail. The validated model can also be used to predict the performance of the basic radar and explore the benefits and limitations of (modelled) hardware changes and processing chain optimisations. The radar model has the potential to be developed as a digital twin to test any hypothetical real radar scenarios within the simulation. One of the interesting aspects would be to explore the limitation of the classical radar oscillator phase noise in target detection and the potential of using a quantum oscillator with better phase noise performance as a suitable alternative [37].

AUTHOR CONTRIBUTIONS

Jithin Kannanthara: Conceptualisation, Data curation, Formal analysis, Investigation, Methodology, Software, Validation, Visualisation, Writing—original draft, Writing—review & editing. **Darren Griffiths**: Conceptualisation, Data curation, Formal analysis, Investigation, Validation, Writing—review & editing. **Mohammed Jahangir**: Conceptualisation, Data curation, Supervision, Writing—review & editing. **Jonathan M. Jones**: Project administration, Supervision, Writing—review & editing. **Christ J. Baker**: Conceptualisation, Funding acquisition, Methodology, Supervision, Writing—review & editing. **Michail Antoniou**: Funding acquisition, Project administration, Supervision. **Colin J. Bell**: Formal analysis, Funding acquisition, Methodology, Supervision, Validation, Writing—review & editing. **Henry White**. Funding acquisition, Supervision, Writing—review & editing. **Kai Bongs**. Funding acquisition, Supervision. **Yeshpal Singh**: Conceptualisation, Funding acquisition, Methodology, Supervision, Writing—review & editing.

ACKNOWLEDGEMENTS

This work was partly supported by the UK National Quantum Technology Hub in Sensing and Timing (Project EP/T001046/1), European Union's Horizon 2020 research and innovation programme (820404—IQ clock project), and BAE Systems I-CASE PhD. The authors would also like to thank Bill Stafford and Caitlin Percy (ex-members of BAE systems). Additionally, the authors would also like to thank Stephen Harman (Aveillant) and Aveillant Ltd.

CONFLICT OF INTEREST STATEMENT

The authors declare that there is no conflict of interest.

DATA AVAILABILITY STATEMENT

Data available on request from the authors.

ORCID

Jithin Kannanthara https://orcid.org/0000-0002-6156-1181

REFERENCES

1. Doviak, R.J., Zrnic, D.S., Sirmans, D.S.: Doppler weather radar. Proc. IEEE 67(11), 1522–1553 (1979). https://doi.org/10.1109/proc.1979.11511
2. Liu, B., et al.: Characteristics and performance of wind profiles as observed by the radar wind profiler network of China. Atmos. Meas. Tech. 13(8), 4589–4600 (2020). https://doi.org/10.5194/amt-13-4589-2020
3. Mercuri, M., et al.: Digital linear discrete FMCW radar for healthcare applications. In: 2019 IEEE MTT-S International Microwave Symposium (IMS), pp. 144–147 (2019)
4. Gu, C., Li, C.: From tumor targeting to speech monitoring: accurate respiratory monitoring using medical continuous-wave radar sensors. IEEE Microw. Mag. 15(4), 66–76 (2014)
5. Li, C., et al.: A review on recent advances in Doppler radar sensors for noncontact healthcare monitoring. IEEE Trans. Microw. Theor. Tech. 61(5), 2046–2060 (2013). https://doi.org/10.1109/tmtt.2013.2256924
6. Carter, L.M., Campbell, D.B., Campbell, B.A.: Geologic studies of planetary surfaces using radar polarimetric imaging. Proc. IEEE 99(5), 770–782 (2011). https://doi.org/10.1109/jproc.2010.2099090
7. Moreira, A., et al.: A tutorial on synthetic aperture radar. IEEE Geosci. Rem. Sens. Mag. 1(1), 6–43 (2013). https://doi.org/10.1109/mgrs.2013.2248301
8. Adnan, M.A., et al.: Vehicle speed measurement technique using various speed detection instrumentation. In: 2013 IEEE Business Engineering and Industrial Applications Colloquium (BEIAC), pp. 668–672 (2013)
9. Ghadaki, H., Dizaji, R.: Target track classification for airport surveillance radar (ASR). In: 2006 IEEE Conference on Radar, pp. 4 (2006)
10. Yang, Y., et al.: Effects of k distributed sea clutter and multipath on radar detection of low altitude sea surface targets. IET Radar Sonar Navig. 8(7), 757–766 (2014). https://doi.org/10.1049/iet-rsn.2013.0285
11. Zhang, S., et al.: Target detection for multistatic radar in the presence of deception jamming. IEEE Sensor. J. 21(6), 8130–8141 (2021). https://doi.org/10.1109/jsen.2021.3050008
12. Björklund, S.: Target detection and classification of small drones by boosting on radar micro-Doppler. In: 2018 15th European Radar Conference (EuRAD), pp. 182–185 (2018)
13. Jahangir, M., Baker, C.: Persistence surveillance of difficult to detect micro-drones with l-band 3-d holographic radar™. In: 2016 CIE International Conference on Radar (RADAR), pp. 1–5 (2016)
14. Siddiq, K., et al.: Phase noise in FMCW radar systems. IEEE Trans. Aerosp. Electron. Syst. 55(1), 70–81 (2018). https://doi.org/10.1109/taes.2018.2847999
15. Siddiq, K., et al.: Phase noise analysis in FMCW radar systems. In: 2015 European Microwave Conference (EuMC), pp. 1523–1526 (2015)
16. Brunner, D., et al.: Radar imaging simulation for urban structures. Geosci. Rem. Sens. Lett. IEEE 8(1), 68–72 (2010). https://doi.org/10.1109/lgrs.2010.2051214
17. Griffiths, H., et al.: Measurement and modelling of bistatic radar sea clutter. IET Radar Sonar Navig. 4(2), 280–292 (2010). https://doi.org/10.1049/iet-rsn.2009.0124

18. Grosdidier, S., Baussard, A., Khenchaf, A.: HFSW radar model: simulation and measurement. IEEE Trans. Geosci. Rem. Sens. 48(9), 3539–3549 (2010). https://doi.org/10.1109/tgrs.2010.2047022
19. Watts, S., Rosenberg, L.: A comparison of coherent and non-coherent radar detection performance in radar sea clutter. In: International Conference on Radar Systems (Radar 2017), pp. 1–6 (2017)
20. Watts, S.: Modeling and simulation of coherent sea clutter. IEEE Trans. Aerosp. Electron. Syst. 48(4), 3303–3317 (2012). https://doi.org/10.1109/taes.2012.6324707
21. Huang, H., Pan, M., Lu, Z.: Hardware-in-the-loop simulation technology of wide-band radar targets based on scattering center model. Chin. J. Aeronaut. 28(5), 1476–1484 (2015). https://doi.org/10.1016/j.cja.2015.07.006
22. Yu, D., et al.: An incoherent scatter radar simulation system based on MATLAB. Geosci. Rem. Sens. Lett. IEEE 17(9), 1513–1517 (2019). https://doi.org/10.1109/lgrs.2019.2950417
23. Al Zubaidy, M.A., Sayidmarie, K.H., Al Shamaa, S.S.: Radar system simulator using pc and MATLAB Simulink. In: 2006 International Radar Symposium, pp. 1–4. IEEE (2006)
24. Brooker, M., Inggs, M.: A signal level simulator for multistatic and netted radar systems. IEEE Trans. Aerosp. Electron. Syst. 47(1), 178–186 (2011). https://doi.org/10.1109/taes.2011.5705668
25. Robins, W.P.: Phase Noise in Signal Sources: Theory and Applications, vol. 9. IET (1984)
26. Gamekeeper Aveillant 16 U. (2020). https://www.aveillant.com/products/gamekeeper/
27. Moran, B.: Mathematics of radar. In: Twentieth Century Harmonic Analysis—A Celebration, pp. 295–328. Springer (2001)
28. Richards, M.A., et al.: Principles of Modern Radar, vol. 1. Citeseer (2010)
29. Mazda, F.: Telecommunications Engineer's Reference Book. Butterworth-Heinemann (2014)
30. Zumbahlen, H., et al.: Linear Circuit Design Handbook. Newnes (2011)
31. Li, C., et al.: Principles and Applications of RF/Microwave in Healthcare and Biosensing. Academic Press (2016)
32. Chen, W.K.: The Electrical Engineering Handbook. Elsevier (2004)
33. Lyon, D.A.: The discrete Fourier transform, part 4: spectral leakage. J. Object Technol. 8(7), 23 (2009). https://doi.org/10.5381/jot.2009.8.7.c2
34. Enggar, F.D., et al.: Performance comparison of various windowing on Fmcw radar signal processing. In: 2016 International Symposium on Electronics and Smart Devices (ISESD), pp. 326–330 (2016)
35. Prabhu, K.M.: Window Functions and Their Applications in Signal Processing. Taylor & Francis (2014)
36. Mohajerin, N., et al.: Feature extraction and radar track classification for detecting uavs in civillian airspace. In: 2014 IEEE Radar Conference, pp. 0674–0679 (2014)
37. Jahangir, M., et al.: Development of quantum enabled staring radar with low phase noise. In: 2021 18th European Radar Conference (EuRAD), pp. 225–228. IEEE (2022)

How to cite this article: Kannanthara, J., et al.: Whole system radar modelling: simulation and validation. IET Radar Sonar Navig. 17(6), 1050–1060 (2023). https://doi.org/10.1049/rsn2.12399